PNAS RESEARCH ARTICLE | PHYSICS

Imaging the Meissner effect in lanthanum hydride using diamond quantum sensors

Yang Chen[a,1], Junyan Wen[a,b,1], Ze-Xu He[a,b,1], Jing-Wei Fan[c], Xin-Yu Pan[a,b], Cheng Ji[d,e], Huiyang Gou[e], Xiaohui Yu[a,b,2], Liucheng Chen[a,2], and Gang-Qin Liu[a,b,2]

Affiliations are included on p. 7.

Edited by J. C. Séamus Davis, University of Oxford, Oxford, United Kingdom; received December 22, 2025; accepted August 11, 2026

Lanthanum hydride has attracted significant attention in recent years due to its signatures of superconductivity at around 250 K. However, the required megabar pressures present extraordinary challenges in verifying its Meissner effect. Although nitrogen-vacancy (NV) centers in diamond offer a solution, their application has been limited by insufficient working pressures. In this work, using a gaseous pressure-transmitting medium, the working pressure of NV centers is extended to nearly 180 GPa. With this quantum probe, magnetic field screening and the Meissner effect of lanthanum hydride are observed at around 240 K and 155 GPa, consistent with the record high transition temperature (T_c) of LaH_{10}. Additionally, spatially resolved measurements reveal significant inhomogeneities within an insufficiently annealed sample, which has a lower T_c of approximately 220 K. Independent X-ray diffraction measurements indicate that this T_c could originate from the $LaH_{9.5\pm\delta}$ $Fm\bar{3}m$ phase. Our work provides experimental evidence for superconductivity in lanthanum hydride and highlights the importance of spatially resolved techniques in characterizing and optimizing samples under ultrahigh pressure conditions.

lanthanum hydride | the Meissner effect | quantum sensing | nitrogen-vacancy centers

Significance

Near-room-temperature superconductivity in hydrogen-rich materials has attracted considerable interest in recent years. However, its characterization is often hindered by the requirement for ultrahigh pressure conditions. This study extends the operational pressure range of diamond nitrogen-vacancy centers to nearly 180 GPa, enabling in situ quantum sensing of superconductivity in lanthanum hydride at almost 240 K. Microscale magnetic imaging reveals sample inhomogeneities and provides a quantitative basis for optimizing hydride superconductors. This work demonstrates that practical quantum advantage can be achieved under harsh conditions, which is important for both quantum technology and quantum materials.

In recent years, compressed hydrides have attracted significant attention as promising candidates for room-temperature superconductors due to the high-frequency phonons of hydrogen and the chemical precompression from the hydrogen sublattice (1–3). A wide range of superconducting hydrides have been successfully synthesized in experiments, spanning binary, ternary, and even quaternary systems, such as H_3S (3), LaH_{10} (4, 5), CaH_6 (6), YH_9 (7), $LaBeH_8$ (8), (Y,Ce)H_9 (9), and (La,Y,Ce)H_{10} (10). However, there is growing skepticism in this field about whether high-pressure hydrides host superconductivity (11, 12). The main challenge arises from the fact that only limited characterization methods are available under megabar pressures, especially for measuring magnetic properties (13). The widely used SQUID and a.c. magnetic susceptibility methods measure the magnetic response of the entire diamond anvil cell (DAC) (14–16). Consequently, the weak diamagnetic signal from the tiny sample is easily overwhelmed by the substantial background from the DAC. Furthermore, these methods generally provide global information about the sample, lacking spatial resolution, which is crucial for understanding the homogeneity of the hydride sample.

With exceptional magnetic sensitivity, submicron spatial resolution, and notably wide working ranges, quantum sensing using diamond nitrogen-vacancy (NV) centers offers an ideal solution to this problem. In-situ magnetic field imaging can be achieved by combining optically detected magnetic resonance (ODMR) with DAC-based high-pressure techniques, and quantum control of NV spins has been demonstrated (17–21). Recently, the working pressure of NV centers has been increased to around 140 GPa (22–25), and this method has been used to probe the Meissner effect in CeH_9 (25) and bilayer nickelate superconductors (26–28) under high pressures. Despite these advances, the working pressure of NV centers is still insufficient to study most hydride superconductors. For example, the superconducting transition temperature (T_c) and required pressure for typical hydrides are H_3S (203 K, 150 GPa) (3), CaH_6 (215 K, 172 GPa) (6), YH_9 (243 K, 201 GPa) (7). The record-high T_c of LaH_{10} (250 to 260 K) is measured under pressures of 150 to 200 GPa (4, 5). To investigate these hydride superconductors, it is essential to further increase the working pressure of diamond NV centers.

In this work, we extend the working pressure of NV centers to nearly 180 GPa by using a gaseous pressure-transmitting medium, thereby reaching the pressures required for most hydride superconductors. Leveraging this capability, we perform in-situ magnetic

Author contributions: X.Y., L.C., and G.-Q.L. designed the research; Y.C., J.W., Z.-X.H., J.-W.F., C.J., H.G., and L.C. performed the research; Y.C., Z.-X.H., and L.C. analyzed the data; and Y.C., L.C., and G.-Q.L. wrote the paper.

The authors declare no competing interest.

This article is a PNAS Direct Submission.

[1]Y.C., J.W., and Z.-X.H. contributed equally to this work.

[2]To whom correspondence may be addressed. Email: yuxh@iphy.ac.cn, chenliucheng@iphy.ac.cn, or gqliu@iphy.ac.cn.

This article contains supporting information online at https://www.pnas.org/lookup/suppl/doi:10.1073/pnas.2536915123/-/DCSupplemental.

Published September 11, 2026.

measurements on lanthanum hydride samples synthesized by laser heating lanthanum and ammonia borane (H_3NBH_3). For a well-annealed sample, unambiguous magnetic field screening and the Meissner effect are observed at 155 GPa, with a transition temperature of 237 K, suggesting that the dominant phase in this sample is LaH_{10}. For an insufficiently annealed sample, magnetic field screening and flux trapping are also observed, with a lower transition temperature of approximately 190 to 220 K. Additionally, spatially resolved measurements reveal significant inhomogeneities within this sample. Synchrotron X-ray diffraction (XRD) and electrical measurements on a separate sample suggest that this T_c corresponds to the $LaH_{9.5\pm\delta}$ $Fm\bar{3}m$ phase. These results show that NV-based quantum sensing is a powerful tool for studying quantum materials at ultrahigh pressures.

Results

Quantum Control at Nearly 180 GPa. Our primary goal is to extend the working pressure range of NV centers in diamond. To generate and maintain high pressures up to nearly 180 GPa, DACs with small culets (60 μm in diameter) are used. A layer of shallow NV centers is created on the (111)-cut diamond anvils through nitrogen ion implantation (20 keV and 2×10^{14} cm^{-2} dose) and followed by annealing under vacuum, as shown in Fig. 1*A*. Previous studies have shown that a uniform and hydrostatic pressure environment is crucial for maintaining the optical readout mechanism of NV spins (22–25). Therefore, we use neon-gas as the pressure-transmitting medium in the experiment, as it provides better hydrostatic pressure conditions than solids. The experiments are performed on a home-built ODMR setup; details of the experimental setup and methods are provided in *Materials and Methods*.

Fig. 1*B* shows a typical confocal image of the diamond culet after compressing the DAC1 sample to 138 GPa; the fluorescence from the NV centers, the platinum wires, and the edge of the diamond culet can be clearly distinguished. Fig. 1*C* presents typical ODMR spectra of NV centers at different pressures. Although broadening and additional splitting appear at higher pressures, the ODMR contrast remains visible up to 179 GPa. By fitting the spectra with single or double Lorentzian functions, the zero-field splitting D is extracted and plotted in Fig. 1*D*. This parameter increases linearly with pressure (coefficient = 8.33 ± 0.08 MHz/GPa), and can therefore serve as an independent criterion for pressure calibration. When an external magnetic field H_z is applied, the ODMR spectrum exhibits two distinct resonances, resulting from the Zeeman splitting between the $|m_s = \pm 1\rangle$ states of the NV centers, as shown in Fig. 1*E*. The external magnetic field can effectively suppress ODMR broadening caused by the pressure gradient. A sharp ODMR signal with a width of about 29 MHz is obtained under an external field of 301 G. Under the same conditions, we measure the Rabi oscillations of NV centers, as shown in Fig. 1*F*, demonstrating that full quantum control is achievable at high pressures near 180 GPa.

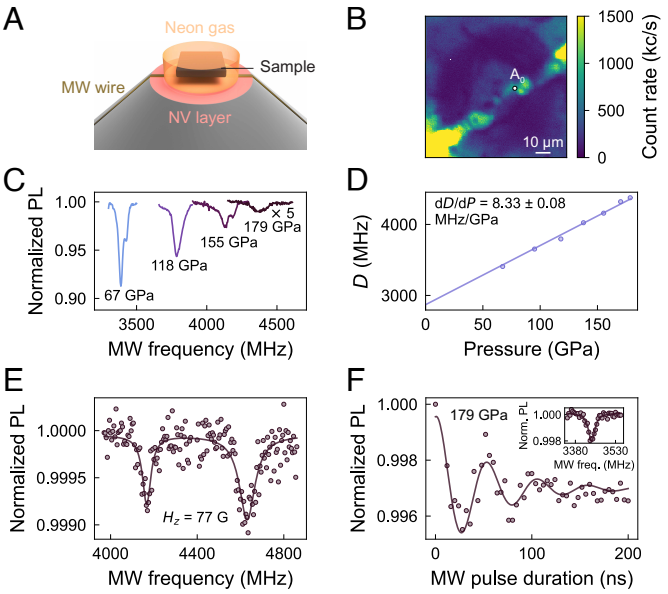

Fig. 1. Quantum control of nitrogen-vacancy (NV) centers in diamond at nearly 180 GPa (DAC1). (*A*) Schematic of the high-pressure chamber. A layer of NV centers is created on the diamond anvil by nitrogen ion implantation followed by high-temperature annealing. Optical excitation and fluorescence collection of the NV centers are performed through the transparent diamond window, while microwave pulses are applied via Pt wires placed on the culet. Neon gas is used as the pressure transmitting medium. (*B*) Confocal image of the diamond culet at $P = 138$ GPa; the measured point is marked as A_0. (*C*) Zero-field optically detected magnetic resonance (ODMR) spectra at different pressures. (*D*) Zero-field splitting, D, as a function of pressure. Pressures are calibrated using the diamond Raman signal (29). (*E*) ODMR spectrum at 179 GPa and $H_z = 77$ G. (*F*) Rabi oscillations of NV centers at 179 GPa and $H_z = 301$ G. *Inset*: ODMR spectra under the same conditions.

Synthesis and Zero-Resistance of Lanthanum Hydride. We then proceed to synthesize and characterize lanthanum hydride at high pressures. Three lanthanum hydride samples (DAC2–4) are synthesized by laser heating lanthanum and ammonia borane; see *Materials and Methods* and *SI Appendix*, Table S1 for details. The DAC2 sample is prepared for electric transport and XRD measurements so (100)-cut diamonds without NV centers are used. DAC3 and DAC4 use (111)-cut diamond anvils with shallow NV centers suitable for subsequent ODMR measurements. The generation of H_2 (*SI Appendix*, Figs. S3*B* and S4*B*) and the decrease in pressure in the high-pressure chamber after laser heating (*SI Appendix*, Fig. S3*A*) indicate that chemical reactions occur in the sample chambers. The H_2 also provides a suitable pressure environment for conducting ODMR measurements under high pressures, similar to the neon gas in the first experiment. In DAC3, the heating laser beam is partially blocked by the Pt wire that delivers microwaves to the NV centers, resulting in an incomplete reaction. In DAC4, this issue is resolved by heating the sample from the opposite side of the DAC, producing a well-annealed sample with a higher T_c of about 240 K.

Synchrotron XRD measurements are conducted to determine the structure of the synthesized products in DAC2. As shown in Fig. 2 *A* and *B*, the sample can be indexed by the space groups of $Fm\bar{3}m$ and $P6_3/mmc$ depending on the structural features reported in similar systems in literature (4, 30). Based on the diffraction peak intensities, $Fm\bar{3}m$ is the primary phase present in this sample (*SI Appendix*, Figs. S5 and S6). The fitted lattice parameters and volumes at selected locations in DAC2 are summarized in *SI Appendix*, Table S2. Although hydrogen occupancy cannot be determined experimentally due to its poor X-ray scattering ability, its concentration can be inferred by comparing the unit cell volume (31, 32). The calculated hydrogen contents are about 8.35 to 9.20 for the $P6_3/mmc$ phase and 9.23 to 9.75 for the synthesized $Fm\bar{3}m$ phases (hereafter labeled as $LaH_{8.8\pm\delta}$ and $LaH_{9.5\pm\delta}$, respectively). The refined volumes of $Fm\bar{3}m$ and $P6_3/mmc$ collected at the red point of Fig. 2*A* are

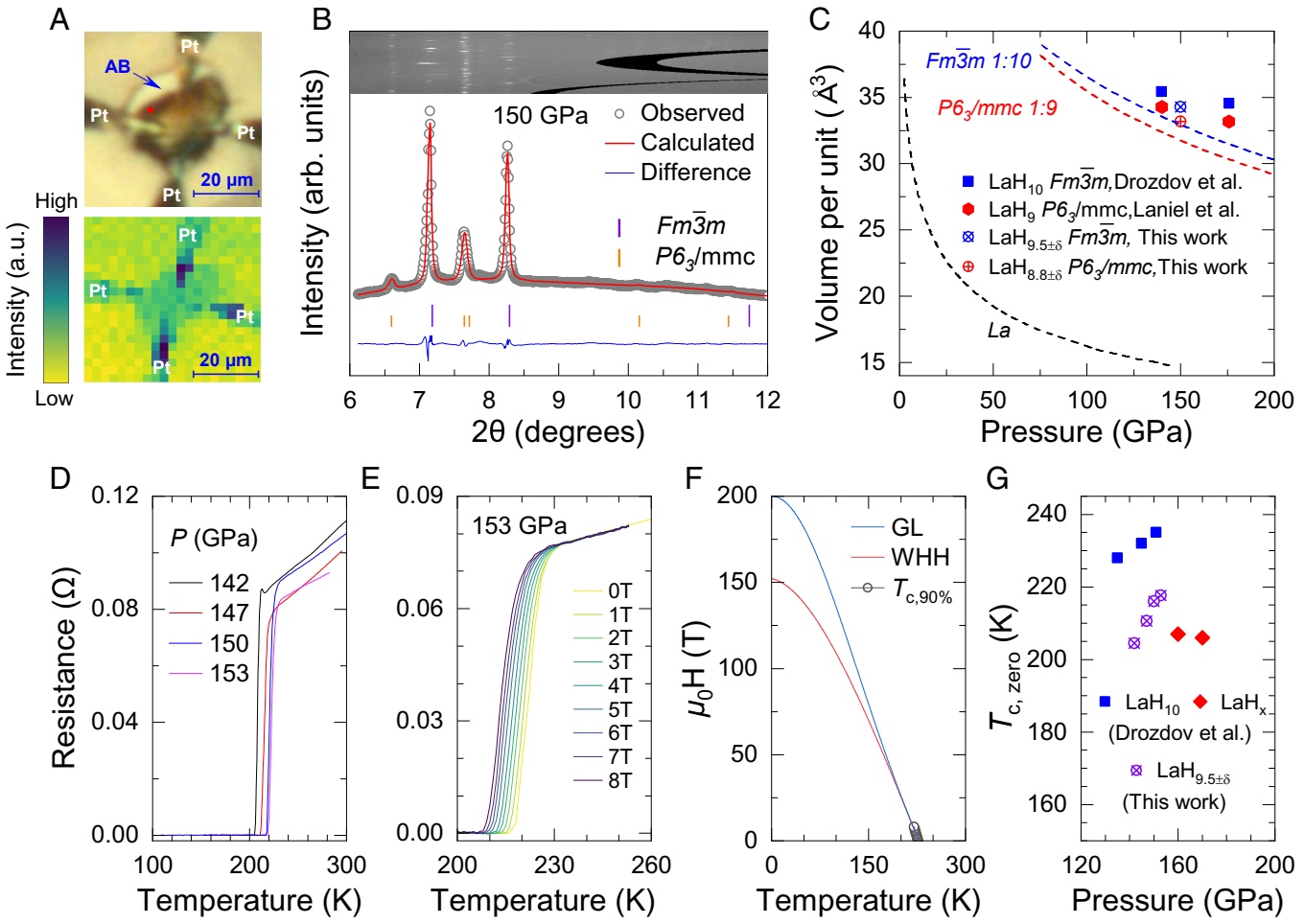

Fig. 2. Synthesis and superconductivity of $LaH_{9.5\pm\delta}$ (DAC2). (*A*) Optical image of the sample chamber after laser heating (*Top*) and the 2 d synchrotron X-ray diffraction (XRD) image of lanthanum hydride at around 150 GPa (*Bottom*). (*B*) XRD data collected at the red point (Fig. 2*A*) along with the model fitting for the phases of $LaH_{9.5\pm\delta}$ $Fm\bar{3}m$ and $LaH_{8.8\pm\delta}$ $P6_3/mmc$. (*C*) Pressure-dependent unit cell volume per lanthanum atom for different lanthanum hydrides. The dashed blue, red, and black lines indicate the pressure–volume (*P–V*) relation of LaH_{10} $Fm\bar{3}m$, LaH_9 $P6_3/mmc$, and La *Fmmm*, respectively. The experimental results for the LaH_{10}, LaH_9, $LaH_{9.5\pm\delta}$, and $LaH_{8.8\pm\delta}$ are shown as blue and red dots. (*D*) Superconducting transitions at different pressures. (*E*) Temperature dependence of the resistance at applied magnetic fields from 0 to 8 T at a pressure of around 153 GPa. (*F*) Upper critical field H_{c2} as a function of temperature, fitted with the Ginzburg–Landau (GL) and Werthamer–Helfand–Hohenberg (WHH) model. (*G*) Pressure dependence of $T_{c,zero}$ for $LaH_{9.5\pm\delta}$ synthesized in this work compared with that of LaH_{10} and LaH_x reported in ref. 4.

shown in Fig. 2*C*, compared with the previously reported *P–V* results of LaH_{10} and LaH_9 (4, 30). The calculated hydrogen concentration of $Fm\bar{3}m$ in this work shows a small deviation from the ideal value of 10, possibly due to the formation of hydrogen vacancies during the synthesis process.

The superconductivity of the synthesized sample in DAC2 is confirmed by electrical transport measurements. The temperature-dependent resistance data at different pressures and under various external magnetic fields are shown in Fig. 2 *D* and *E*, respectively. Sharp superconducting transitions and zero resistance are clearly observed. These results indicate that the observed superconductivity arises from a single phase. In Fig. 2*E*, the resistance gradually shifts to lower temperatures, and the superconducting transition broadens under strong magnetic fields. As shown in Fig. 2*F*, the upper critical field at 0 K is extrapolated to be 156 and 200 T with the Ginzburg–Landau (GL) and Werthamer–Helfand–Hohenberg (WHH) model fitting (33, 34), respectively. Fig. 2*G* summarizes the extracted $T_{c,zero}$ (the temperature at which the resistance drops to zero) of our sample, along with LaH_{10} and LaH_x reported by Drozdov et al. (4). Given that the reported T_c values of LaH_9 $P6_3/mmc$ and related phases remain significantly below the $T_{c,zero}$ values measured in our sample [*SI Appendix*, Table S3; (35–37)], we conclude that the superconducting phase in DAC2 is $LaH_{9.5\pm\delta}$ $Fm\bar{3}m$.

Magnetic Field Screening and Flux Trapping. We then characterize the diamagnetic properties of lanthanum hydride in DAC3 with integrated quantum sensors. As shown in Fig. 3*A*, the sample region is identified by comparing the confocal image with the bright field image. In the zero-field cooling and field-warming (ZFC-FW) experiment, the sample is first cooled to 100 K at zero field. ODMR spectra are then acquired under a uniform external magnetic field. Typical ODMR spectra and their temperature dependence are shown in Fig. 3 *B–D*. For NV centers far from the sample, such as the C_0 position, a clear two-dip feature with barely temperature dependence is observed (*SI Appendix*, Fig. S7). Therefore, ODMR spectra at this position serve as a reference to estimate the strength of the external magnetic field, which is fixed at 105 G. For NV centers directly below the sample, such as at the C_1 position, a much smaller splitting (242 MHz) is observed, indicating strong magnetic field

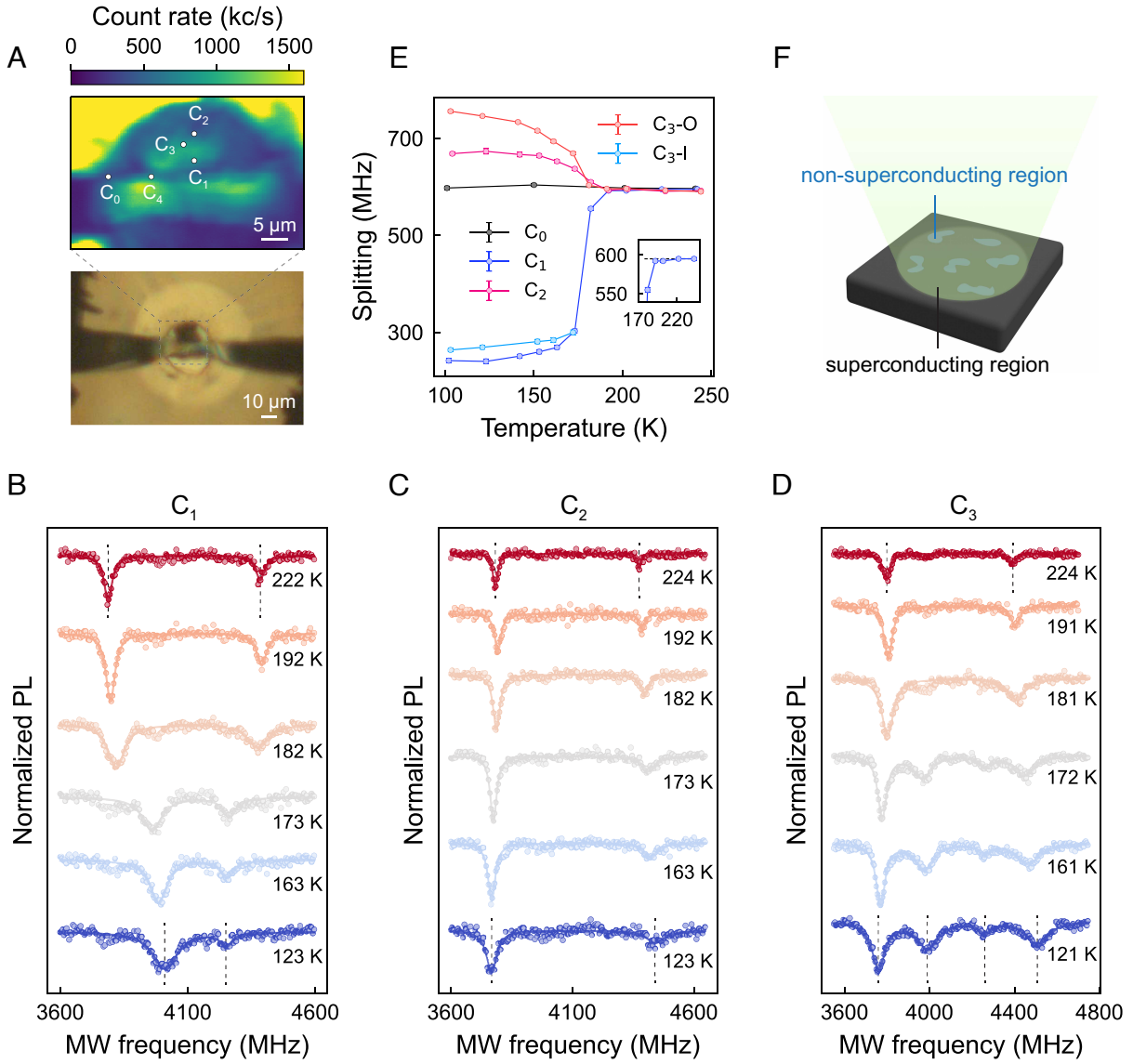

Fig. 3. Magnetic field screening in lanthanum hydride (DAC3). (*A*) Confocal fluorescence image (*Top*) and bright-field image (*Bottom*) of the sample. (*B–D*) ODMR spectra of C_1–C_3 measured during field heating at $H_z = 105$ G after zero-field cooling. The solid lines are fits with multiple Lorentzian functions. At around 120 K, ODMR spectra at C_1 (sample center) and C_2 (near the sample edge) reveal strong diamagnetism and concentration of magnetic flux, respectively. Most other test points (C_3 and more data in *SI Appendix*, Fig. S8) show both effects simultaneously–four dips are observed at low temperatures, and ODMR splitting extracted from the outer (inner) dips decreases (increases) with temperature. At around 220 K, all ODMR spectra display a two-dip feature with identical splitting determined by the external magnetic field. (*E*) ODMR splittings of the examined points as a function of temperature. The outer and inner pairs of dips in the ODMR spectra of C_3 are labeled C_3-O and C_3-I, respectively. (*F*) Schematic illustrating the coexistence of superconducting and nonsuperconducting regions in the laser-focused area, which produces four-dip ODMR spectra when NV centers of a single orientation are involved.

screening from the sample. As temperature increases, a sharp transition of the ODMR splitting is observed, from which a T_c of approximately 190 to 220 K can be estimated (Fig. 3*E*). In contrast, for NV centers near the sample edge (C_2), ODMR splittings are larger at temperatures below T_c, and gradually decrease to the reference value. The initially larger splitting is attributed to the concentration of magnetic flux repelled from the superconducting regions. At temperatures above 220 K, ODMR splittings at different positions converge to nearly the same value.

An interesting finding in this sample is that many of the examined points display a four-dip feature in their ODMR spectra, as shown in Fig. 3*D* and *SI Appendix*, Fig. S8. Since the experiment is conducted at a high pressure of 135 GPa, only NV centers in the (111) orientation can survive (24, 25), and a specific magnetic field splits the resonance dip into two. The four-dip feature at low temperatures indicates that the NV centers in the detection volume experience two primary magnetic fields. Note that the optical resolution of our system (approximately 2 μm) is on the same order as the NV center–sample distance. Tracking the temperature dependence of these four dips reveals that the inner pair exhibits local diamagnetism, while the outer pair behaves similarly to C_2 (Fig. 3*E*). The four-dip ODMR spectra and their temperature dependence suggest that both superconducting and nonsuperconducting regions exist in the detection volume and contribute to the ODMR signals, as illustrated in Fig. 3*F*.

Flux trapping in DAC3 is investigated by measuring zero-field ODMR spectra after field cooling (105 G) the sample to 100 K. A second round of measurement is performed after zero-field cooling for comparison. Typical ODMR spectra are shown in

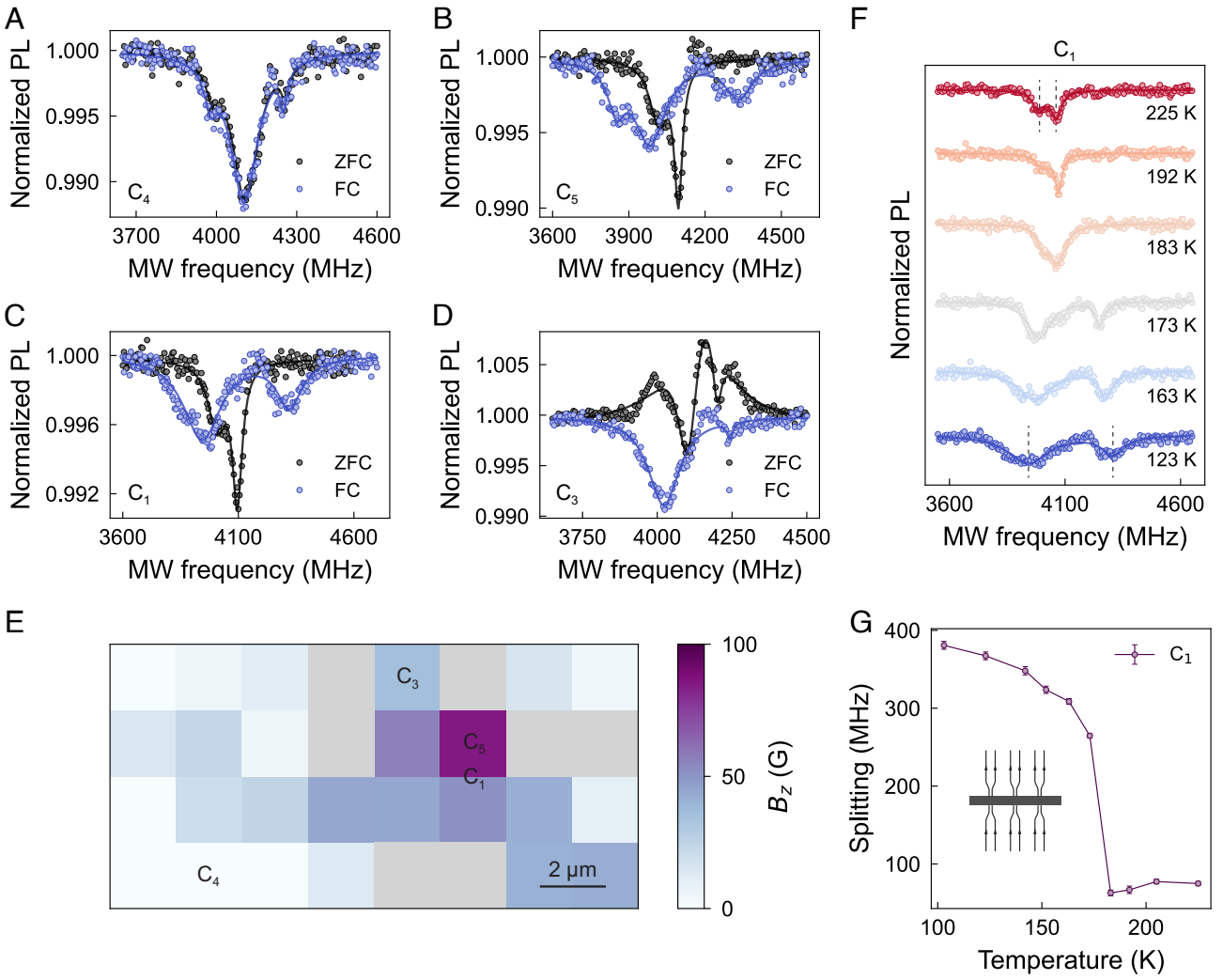

Fig. 4. Imaging flux trapping using in-situ quantum sensors (DAC3). (*A–D*) Zero-field ODMR spectra of four representative points (C_4, C_5, C_1, and C_3) measured after zero-field cooling and field cooling at $H_z = 105$ G. The solid lines are fits with multiple Lorentzian functions. For NV centers at C_4, the two ODMR signals are nearly identical, indicating no flux trapping at this position. In contrast, most other measured points exhibit very different zero-field ODMR spectra after field cooling, indicating strong local flux trapping at these positions. (*E*) Spatial map of the residual magnetic field B_z. The center of the sample shows strong flux trapping. Positions with finite trapped field B_z, whose magnitude cannot be estimated, are marked in gray (*SI Appendix*, Fig. S10). (*F*) ODMR spectra of C_1 measured during zero-field heating after field cooling at $H_z = 105$ G. (*G*) ODMR splittings of C_1 as a function of temperature. *Inset*: Sketch of flux trapping.

Fig. 4 *A–D*. At C_4, the ODMR spectra from field cooling and zero-field cooling are nearly identical, indicating that no flux trapping occurred at this position. In contrast, the ODMR spectra at C_5 and C_1 (and many other positions) after field cooling show significantly larger splitting compared to their ZFC counterparts, as shown in Fig. 4 *B* and *C*. The broadened resonant dips indicate strong magnetic field gradients at these positions. To further verify that the residual magnetic field results from flux trapping in the superconducting sample, we gradually warm the sample and measure ODMR spectra at C_1, as shown in Fig. 4*F*. The ODMR splitting decreases as temperature increases and eventually returns to the intrinsic value, indicating that the trapped flux is released (Fig. 4*G*).

The high spatial resolution of diamond quantum sensing enables us to image flux trapping under megabar pressures. To quantify the trapped flux, all measured ODMR spectra are fitted with multiple Lorentzian functions. The outermost pair of dips is used to estimate the strength of the residual magnetic field due to flux trapping. The axial trapped field B_z is obtained by subtracting (in quadrature, see *Materials and Methods* for details) the ZFC splitting from the FC splitting. For certain points, such as C_3, the ODMR spectrum displays an additional positive envelope (Fig. 4*D*), possibly due to nonaxial stress at the location (38). Nevertheless, their magnetic field dependence is similar to that of the normal ODMR spectra (competition between the Zeeman effect and transverse stress; *SI Appendix*, Fig. S9). The results from all measured points, which provide a spatial map of the axial trapped field B_z, are shown in Fig. 4*E*. Interestingly, positions with strong flux trapping signals, such as C1 and C3, also show strong magnetic field screening. This observation is consistent with flux trapping in CeH_9 superconductors under high pressure (25). The variation in flux trapping among the positions, along with the four-dip feature observed in the ZFC-FW experiment (Fig. 3*D*), indicates significant inhomogeneity in the DAC3 sample. We attribute this to insufficient annealing, as the microwave wire partially blocks the heating laser beam during synthesis.

Meissner Effect in Lanthanum Hydride. We then examine the diamagnetism of lanthanum hydride in the well-annealed DAC4 sample. First, ZFC-FW measurements are conducted to verify the magnetic screening effect. The sample is cooled to 60 K, and

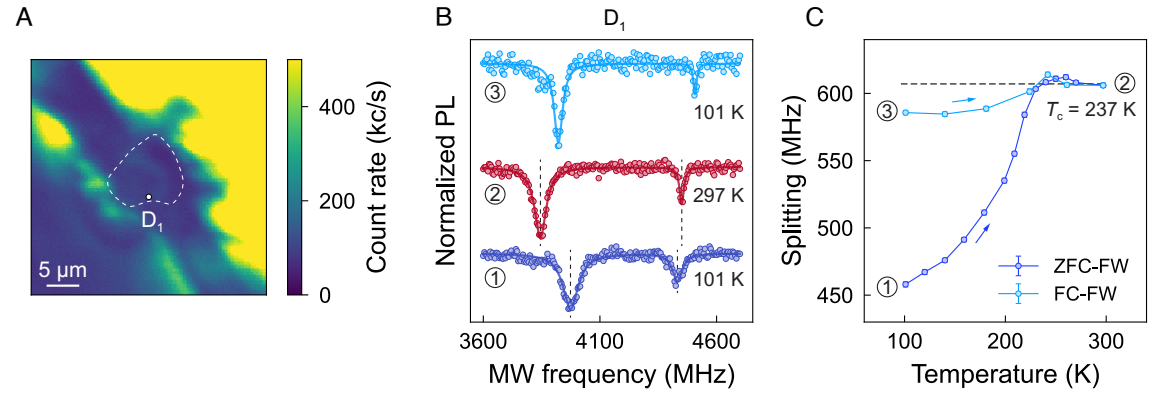

Fig. 5. Meissner effect in lanthanum hydride at 155 GPa (DAC4). (*A*) Confocal fluorescence image of the lanthanum hydride sample (DAC4) at $P = 155$ GPa; the measured point is marked as D_1. The approximate sample boundary is indicated by the dashed contour. (*B*) ODMR spectra of D_1 measured during field warming at $H_z = 105$ G after zero-field cooling (ZFC-FW; ① and ②) or field cooling (FC-FW; ③). Clear diamagnetism is observed by comparing the two splittings in the ZFC-FW cycle. (*C*) ODMR splittings of D_1 as a function of temperature, from which a transition temperature of $T_c = 237$ K is determined; see *Methods* for details.

ODMR spectra are measured under an external magnetic field of $H_z = 105$ G. Clear local diamagnetism (e.g., D_1 in Fig. 5*A*) is observed in this sample. Typical ODMR spectra are shown in Fig. 5*B*. By tracking the temperature dependence of the ODMR splitting, a transition temperature T_c of 237 K is determined, as shown in Fig. 5*C*, see *Materials and Methods* for details. This high T_c is close to previously reported values for the LaH_{10} phase (240 to 255 K) (4), suggesting that the dominant phase in this sample is LaH_{10}.

The Meissner effect in this sample is further confirmed by the field cooling-field warming (FC-FW) experiment. A fixed and uniform external magnetic field, $H_z = 105$ G, is applied throughout the measurement. At 297 K, the ODMR spectrum measured at D_1 shows a splitting of 606 MHz. The sample is then cooled to 101 K, where a smaller ODMR splitting of 586 MHz is observed at the same position. This signal indicates that the local magnetic field is spontaneously expelled at the measured position, a clear signature of the Meissner effect. Next, by gradually warming the sample, the ODMR splitting returns to the value observed in the normal state, as shown in the sky blue curve of Fig. 5*C*. The diamagnetic effect in the FC-FW measurement is notably smaller than in the ZFC-FW measurement, indicating that part of the external magnetic field penetrates into the sample during field cooling.

Discussion

A comparison of the ODMR results from DAC3 and DAC4 provides insights into optimizing lanthanum hydride superconductors. Both samples exhibit clear magnetic field screening effects, but their homogeneity and T_c differ. The well-annealed sample in DAC4 has a much higher T_c and better homogeneity, indicating that sufficient annealing is essential for synthesizing the LaH_{10} phase. Notably, the relative change in ODMR splitting during the ZFC-FW measurement for DAC4 (24%) is considerably smaller than for DAC3 (59%). This difference can be explained by the relative position of the NV centers with respect to the superconducting sample. At position D1 in DAC4, the microwave wire and pressure-transmitting medium (about 1 μm thick) lie between the NV centers and the sample. In contrast, at position C1 in DAC3, no such wire is present, so the NV centers should be closer to the sample and detect a stronger diamagnetic signal.

In summary, this work provides experimental evidence of magnetic field screening, flux trapping, and the Meissner effect in lanthanum hydride superconductors under megabar pressures. Compared to conventional probes (16), NV centers offer spatially resolved demagnetization signals of the lanthanum hydride sample, enabling the investigation of sample inhomogeneities at the microscale, which is crucial for optimizing the synthesis of hydride superconductors under high pressures. With this method, magnetic susceptibility can be determined by measuring how the local magnetization varies with the applied external field, provided that both the NV–sample distance and the sample geometry are accurately known. Furthermore, by mapping and integrating the magnetic signal across the entire sample, one can estimate the superconducting volume fraction, a widely used metric and key indicator of sample quality. Our work also demonstrates the functionality of NV quantum sensors at pressures up to nearly 180 GPa, with significant potential to further increase the working pressure of NV centers in diamond. Looking forward, the combination of high pressure with other conditions, such as strong magnetic fields, ultra-low temperatures, or high temperatures, offers opportunities to identify and understand quantum states under synergetic extreme conditions. By leveraging advanced quantum control and quantum properties of NV centers (39–42), practical quantum advantage can be achieved under extreme conditions.

Materials and Methods

Fabrication of NV Centers and Sample Loading. Four nonmagnetic symmetric DACs (DAC1–4) were prepared to generate high pressures. The pressure was determined from the first-order Raman spectra of the diamond anvils (29, 43). The diamonds used in the DACs had 50, 60, or 80 μm culets and were beveled at 8 to 8.5° to a diameter of about 300 μm. The top anvils of DAC1, DAC3, and DAC4 were (111)-cut diamonds (type Ib for DAC1 and type IIa for DAC3 and DAC4), which were implanted with a layer of NV centers. To create the NV layer, the diamonds were implanted with N^+ ions at 20 keV and a dose of 2×10^{14} cm^{-2} and subsequently annealed at 800 °C for 2 h. All the other anvils were (100)-cut diamonds. In DAC1, a 40 μm hole was laser drilled to serve as the sample chamber and then prefilled with a mixture of cubic boron nitride (cBN) and epoxy to electrically isolate the rhenium gasket. A thin platinum foil (1 μm thick × 5 μm wide) was positioned on the diamond culet for microwave transmission. Finally, neon gas was loaded into the sample chamber as the pressure-transmitting medium to provide better hydrostatic conditions.

Synthesis of Lanthanum Hydride. For DAC2–4, samples were loaded in an argon-filled glovebox (O_2 and $H_2O < 0.1$ ppm) to avoid air exposure. A 1 to 2 μm thick lanthanum piece was placed in direct contact with ammonia borane (H_3NBH_3), which served as both the hydrogen source and the pressure-transmitting medium (9). A similar platinum foil was positioned as described above in DAC1. After sealing, the DAC was compressed in multiple steps to the target pressure required to synthesize lanthanum hydrides. The sample was then laser-heated from one-side to 1,500 to 2,000 K for 1 to 2 min using a yttrium-aluminum-garnet (YAG) laser. A laser power of 15 W was used and focused onto a spot of approximately 5 μm.

ODMR Measurements. ODMR measurements were performed on a home-built confocal microscope system equipped with a commercial cryostat (s100, Montana Instruments). A 532-nm laser (CNI Laser) was focused by a long working distance objective (LT-APO/ULWD/VISIR/0.35, attocube) to initialize the NV centers. The emitted fluorescence was filtered by a 650-nm longpass filter (Thorlabs) and detected using a single-photon counting module (SPCM-780-10-FC, Excelitas). Laser and microwave pulses were generated with an acousto-optic modulator (Gooch & Housego) and an RF switch (Minicircuits), respectively. Pulse synchronization and countertiming were controlled by a programmable multichannel pulse generator (PBESR-PRO 500, SpinCore). The ODMR spectra were recorded in continuous-wave mode, with laser excitation, microwave driving, and photon counting performed simultaneously while sweeping the microwave frequency.

Electrical Transport Measurements. A typical symmetric DAC (DAC2) made from Cu-Be alloy was used for electrical transport measurements at external magnetic fields ranging from 0 to 8 T. For the resistance measurements, the rhenium gasket was insulated with a mixture of cubic boron nitride (cBN) and epoxy. Four platinum electrodes were attached in the chamber to connect the sample to external copper wires using the Van Der Pauw method for resistance measurements at high pressures (44). The measurements were conducted in a commercial cryostat equipped with a Keithley 6221 current source and a 2182A nanovoltmeter.

Synchrotron X-Ray Diffraction Measurements. At high pressures, XRD patterns were collected using DAC2 at the ID27 synchrotron beamline of the European Synchrotron Radiation Facility (Grenoble, France) with the EIGER2 X CdTe 9M detector. The wavelength was set to 0.3738 Å and the spot size was 700 nm. The obtained two-dimensional XRD patterns were integrated into one-dimensional profiles using the DIOPTAS software (45). The data were then analyzed with the JANA software based on the LeBail method (46). We also attempted to collect XRD data for the samples in DAC3 and DAC4, but the DACs broke during the XRD experiments.

Determination of T_c from ODMR Splitting. The superconducting transition temperature (T_c) was determined as follows. A horizontal baseline was defined from the average splitting at temperatures well above T_c. As the temperature decreased, T_c was identified as the temperature at which the splitting began to deviate downward from this baseline (Fig. 5*C*). A range was given to DAC3 to account for the sparse data points or possible stress-induced splitting changes (Fig. 3*E*).

Calculation of the Axial Trapped Field B_z. In the absence of external disturbances, the ground-state Hamiltonian of an NV center is given by $H_0 = DS_z^2$. Here, $D \approx (2\pi) \times 2.87$ GHz is the zero-field splitting parameter at ambient conditions, and $\vec{S} = (S_x, S_y, S_z)$ is the spin-1 operator expressed in the local frame of the NV center (z is defined along the NV axis). A magnetic field $\vec{B}$ couples to the NV center through the Hamiltonian $H_B = \gamma_B \vec{B} \cdot \vec{S}$, where $\gamma_B = (2\pi) \times 2.802$ MHz is the gyromagnetic ratio of the NV center (47). Stress couples via the Hamiltonian $H_S = \Pi_z S_z^2 + \Pi_x (S_y^2 - S_x^2) + \Pi_y (S_x S_y + S_y S_x)$, where Π_x, Π_y and Π_z are functions of the stress tensor $\boldsymbol{\sigma}$ (19, 25) Stress components that break the C_{3v} symmetry of the NV center induce a splitting $2\Pi_\perp = 2\sqrt{\Pi_x^2 + \Pi_y^2}$. The Zeemann splitting $2\gamma_B B_z$ from an axial magnetic field B_z adds in quadrature with the stress-induced splitting $2\Pi_\perp$. This results in a total ODMR splitting of $\Delta = \sqrt{(2\gamma_B B_z)^2 + (2\Pi_\perp)^2}$, from which B_z can be extracted. Specifically, the ODMR splittings were extracted by fitting the spectra with multiple Lorentzian functions. For spectra with more than two dips, the outermost pair of dips was used, as it corresponds to the highest typical B_z value.

Data, Materials, and Software Availability. Data for Figs. 1-5 in the main text are openly available at Science Data Bank (48). Data for Figs. S1-S10 are included in the article and/or *SI Appendix*.

ACKNOWLEDGMENTS. This work is supported by the National Key Research and Development Program of China (Grant Nos. 2023YFA1608900, 2021YFA1400300, and 2024YFA1611300), the Quantum Science and Technology-National Science and Technology Major Project (Grant No. 2023ZD0300600), the National Natural Science Foundation of China (Grant Nos. 12022509, T2121001, 12074422, 12374468, 12375304, and 12404163), and the Chinese Academy of Sciences (Grant Nos. XDB33000000 and YSBR-100). We acknowledge the European Synchrotron Radiation Facility for the Synchrotron X-ray diffraction measurements under proposal HC-6177. We thank the high-pressure synergetic measurement station (A9) of the Synergetic Extreme Condition User Facility for assistance with high-pressure resistivity measurements and laser heating. We thank Yue Xu and Rui-Zhi Zhang for fruitful discussions.

Author affiliations: [a]Beijing National Laboratory for Condensed Matter Physics, Institute of Physics, Chinese Academy of Sciences, Beijing 100190, China; [b]School of Physical Sciences, University of Chinese Academy of Sciences, Beijing 100049, China; [c]Department of Physics, Hefei University of Technology, Hefei 230601, China; [d]Shanghai Key Laboratory of MFree, Shanghai Advanced Research in Physical Science, Shanghai 201203, China; and [e]Center for High Pressure Science and Technology Advanced Research, Beijing 100193, China

1. N. W. Ashcroft, Metallic hydrogen: A high-temperature superconductor?. *Phys. Rev. Lett* **21**, 1748 (1968).
2. H. Wang, J. S. Tse, K. Tanaka, T. Iitaka, Y. Ma, Superconductive sodalite-like clathrate calcium hydride at high pressures. *Proc. Natl. Acad. Sci. U.S.A.* **109**, 6463–6466 (2012).
3. A. P. Drozdov, M. I. Eremets, I. A. Troyan, V. Ksenofontov, S. I. Shylin, Conventional superconductivity at 203 kelvin at high pressures in the sulfur hydride system. *Nature* **525**, 73–76 (2015).
4. A. P. Drozdov *et al.*, Superconductivity at 250 K in lanthanum hydride under high pressures. *Nature* **569**, 528–531 (2019).
5. M. Somayazulu *et al.*, Evidence for superconductivity above 260 K in lanthanum superhydride at megabar pressures. *Phys. Rev. Lett.* **122**, 027001 (2019).
6. L. Ma *et al.*, High-temperature superconducting phase in clathrate calcium hydride CaH_6 up to 215 K at a pressure of 172 GPa. *Phys. Rev. Lett.* **128**, 167001 (2022).
7. P. Kong *et al.*, Superconductivity up to 243 K in the yttrium-hydrogen system under high pressure. *Nat. Commun.* **12**, 5075 (2021).
8. Y. Song *et al.*, Stoichiometric ternary superhydride $LaBeH_8$ as a new template for high-temperature superconductivity at 110 K under 80 GPa. *Phys. Rev. Lett.* **130**, 266001 (2023).
9. L. C. Chen *et al.*, Synthesis and superconductivity in yttrium-cerium hydrides at high pressures. *Nat. Commun.* **15**, 1809 (2024).
10. S. Chen *et al.*, Superior superconducting properties realized in quaternary La-Y-Ce hydrides at moderate pressures. *J. Am. Chem. Soc.* **146**, 14105–14113 (2024).
11. J. E. Hirsch, F. Marsiglio, Clear evidence against superconductivity in hydrides under high pressure. *Matter Radiat. Extremes* **7**, 058401 (2022).
12. J. E. Hirsch, Are hydrides under high-pressure-high-temperature superconductors? *Natl. Sci. Rev.* **11**, nwad174 (2024).
13. G. S. Boebinger *et al.*, Hydride superconductivity is here to stay. *Nat. Rev. Phys.* **7**, 2–3 (2025).
14. X. Huang *et al.*, High-temperature superconductivity in sulfur hydride evidenced by alternating-current magnetic susceptibility. *Natl. Sci. Rev.* **6**, 713–718 (2019).
15. V. S. Minkov *et al.*, Magnetic field screening in hydrogen-rich high-temperature superconductors. *Nat. Commun.* **13**, 3194 (2022).
16. V. S. Minkov, V. Ksenofontov, S. L. Bud'ko, E. F. Talantsev, M. I. Eremets, Magnetic flux trapping in hydrogen-rich high-temperature superconductors. *Nat. Phys.* **19**, 1293–1300 (2023).
17. M. W. Doherty *et al.*, Electronic properties and metrology applications of the diamond NV^- center under pressure. *Phys. Rev. Lett.* **112**, 047601 (2014).
18. Y. X. Shang *et al.*, Magnetic sensing inside a diamond anvil cell via nitrogen-vacancy center spins. *Chin. Phys. Lett.* **36**, 086201 (2019).
19. S. Hsieh *et al.*, Imaging stress and magnetism at high pressures using a nanoscale quantum sensor. *Science* **366**, 1349–1354 (2019).
20. M. Lesik *et al.*, Magnetic measurements on micrometer-sized samples under high pressure using designed NV centers. *Science* **366**, 1359–1362 (2019).
21. K. Y. Yip *et al.*, Measuring magnetic field texture in correlated electron systems under extreme conditions. *Science* **366**, 1355–1359 (2019).
22. J. H. Dai *et al.*, Optically detected magnetic resonance of diamond nitrogen-vacancy centers under megabar pressures. *Chin. Phys. Lett.* **39**, 117601 (2022).

23. A. Hilberer *et al*., Enabling quantum sensing under extreme pressure: Nitrogen-vacancy magnetometry up to 130 GPa. *Phys. Rev. B* **107**, L220102 (2023).
24. M. Wang *et al*., Imaging magnetic transition of magnetite to megabar pressures using quantum sensors in diamond anvil cell. *Nat. Commun.* **15**, 8843 (2024).
25. P. Bhattacharyya *et al*., Imaging the Meissner effect in hydride superconductors using quantum sensors. *Nature* **627**, 73–79 (2024).
26. J. Wen *et al*., Imaging the Meissner effect in pressurized bilayer nickelate with integrated multi-parameter quantum sensor. *Natl. Sci. Rev.* **12**, nwaf268 (2025).
27. L. Liu *et al*., Evidence for the Meissner effect in the nickelate superconductor $La_3Ni_2O_{7-\delta}$ single crystal using diamond quantum sensors. *Phys. Rev. Lett.* **135**, 096001 (2025).
28. S. Mandyam *et al*., Uncovering origins of heterogeneous superconductivity in $La_3Ni_2O_7$. *Nature* **651**, 54–60 (2026).
29. Y. Akahama, H. Kawamura, Raman study on the stress state of [111] diamond anvils at multimegabar pressure. *J. Appl. Phys.* **98**, 083523 (2005).
30. D. Laniel *et al*., High-pressure synthesis of seven lanthanum hydrides with a significant variability of hydrogen content. *Nat. Commun.* **13**, 6987 (2022).
31. C. Ji *et al*., Ultrahigh-pressure isostructural electronic transitions in hydrogen. *Nature* **573**, 558–562 (2019).
32. W. Chen *et al*., Superconductivity and equation of state of lanthanum at megabar pressures. *Phys. Rev. B* **102**, 134510 (2020).
33. V. L. Ginzburg, L. D. Landau, On the theory of superconductivity. *Zh. Eksp. Teor. Fiz.* **20**, 1064 (1950).
34. N. R. Werthamer, E. Helfand, P. C. Hohenberg, Temperature and purity dependence of the superconducting critical field, H_{extc2}. I. Electron spin and spin-orbit effects. *Phys. Rev.* **147**, 295 (1966).
35. I. A. Kruglov *et al*., Superconductivity of LaH_{10} and LaH_{16} polyhydrides. *Phys. Rev. B* **101**, 024508 (2020).
36. J. Bi *et al*., Giant enhancement of superconducting critical temperature in substitutional alloy $(La, Ce)H_9$. *Nat. Commun.* **13**, 5952 (2022).
37. P. Dalladay-Simpson *et al*., Raman fingerprint of high-temperature superconductivity in compressed hydrides. arXiv [Preprint] (2025). http://arxiv.org/abs/2511.10784 (Accessed 19 June 2026).
38. Z. Liu *et al*., Strain-engineered nanoscale spin polarization reversal in diamond nitrogen-vacancy centers. *Phys. Rev. Lett.* **136**, 143001 (2026).
39. W. Wu *et al*., Spin squeezing in an ensemble of nitrogen-vacancy centres in diamond. *Nature* **646**, 74–80 (2025).
40. L. Zaporski *et al*., Quantum-amplified global-phase spectroscopy on an optical clock transition. *Nature* **646**, 309–314 (2025).
41. P. Wang, C. Chen, X. Peng, J. Wrachtrup, R. B. Liu, Characterization of arbitrary-order correlations in quantum baths by weak measurement. *Phys. Rev. Lett.* **123**, 050603 (2019).
42. J. Rovny *et al*., Nanoscale diamond quantum sensors for many-body physics. *Nat. Rev. Phys.* **6**, 753–768 (2024).
43. Y. Akahama, H. Kawamura, Pressure calibration of diamond anvil Raman gauge to 310 Gpa. *J. Appl. Phys.* **100**, 043516 (2006).
44. L. J. van der Pauw, A method of measuring specific resistivity and Hall effect of discs of arbitrary shape. *Philips Res. Rep* **13**, 1 (1958).
45. C. Prescher, V. B. Prakapenka, DIOPTAS: A program for reduction of two-dimensional X-ray diffraction data and data exploration. *High Press. Res.* **35**, 223–230 (2015).
46. A. Le Bail, Whole powder pattern decomposition methods and applications: A retrospection. *Powder Diffr.* **20**, 316–326 (2005).
47. J. F. Barry *et al*., Sensitivity optimization for NV-diamond magnetometry. *Rev. Mod. Phys.* **92**, 015004 (2020).
48. G.-Q. L., Data for "Imaging the Meissner effect in lanthanum hydride using diamond quantum sensors". Science Data Bank. https://doi.org/10.57760/sciencedb.46306. Deposited 16 August 2026.